Biomedical Optics EXPRESS

Characterization of a 3D optrode array for infrared neural stimulation

T.V.F. Abaya,[1] M. Diwekar,[1] S. Blair,[1,2,*] P. Tathireddy,[1] L. Rieth,[1] G.A. Clark,[2] and F. Solzbacher[1,2]

[1]*Department of Electrical and Computer Engineering, University of Utah, Salt Lake City, Utah 84112, USA*
[2]*Department of BioEngineering, University of Utah, Salt Lake City, Utah 84112, USA*
[*]*blair@ece.utah.edu*

Abstract: This paper characterizes the Utah Slant Optrode Array (USOA) as a means to deliver infrared light deep into tissue. An undoped crystalline silicon (100) substrate was used to fabricate 10×10 arrays of optrodes with rows of varying lengths from 0.5 mm to 1.5 mm on a 400-μm pitch. Light delivery from optical fibers and loss mechanisms through these Si optrodes were characterized, with the primary loss mechanisms being Fresnel reflection, coupling, radiation losses from the tapered shank and total internal reflection in the tips. Transmission at the optrode tips with different optical fiber core diameters and light in-coupling interfaces was investigated. At $\lambda = 1.55\,\mu$m, the highest optrode transmittance of 34.7%, relative to the optical fiber output power, was obtained with a 50-μm multi-mode fiber butt-coupled to the optrode through an intervening medium of index $n = 1.66$. Maximum power is directed into the optrodes when using fibers with core diameters of 200 μm or less. In addition, the output power varied with the optrode length/taper such that longer and less tapered optrodes exhibited higher light transmission efficiency. Output beam profiles and potential impacts on physiological tests were also examined. Future work is expected to improve USOA efficiency to greater than 64%.

OCIS codes: (170.3890) Medical optics instrumentation; (220.4610) Optical fabrication; (230.7380) Waveguides, channeled; (260.3060) Infrared.

References and links

1. X. Navarro, T. B. Krueger, N. Lago, S. Micera, T. Stieglitz, and P. Dario, "A critical review of interfaces with the peripheral nervous system for the control of neuroprostheses and hybrid bionic systems," J. Peripher. Nerv. Syst. **10**, 229–258 (2005).
2. A. Branner, R. B. Stein, and R. A. Normann, "Selective stimulation of cat sciatic nerve using an array of varying-length microelectrodes," J. Neurophysiol. **85**, 1585–1594 (2001).
3. A. Branner, R. Stein, E. Fernandez, Y. Aoyagi, and R. Normann, "Long-term stimulation and recording with a penetrating microelectrode array in cat sciatic nerve," IEEE T. Bio-Med. Eng. **51**, 146–157 (2004).
4. R. A. Normann, B. R. Dowden, M. A. Frankel, A. M. Wilder, S. D. Hiatt, N. M. Ledbetter, D. A. Warren, and G. A. Clark, "Coordinated, multi-joint, fatigue-resistant feline stance produced with intrafascicular hind limb nerve stimulation," J. Neural Eng. **9**, 026019 (2012).
5. M. Frankel, B. Dowden, V. Mathews, R. Normann, G. Clark, and S. Meek, "Multiple-input single-output closed-loop isometric force control using asynchronous intrafascicular multi-electrode stimulation," IEEE T. Neur. Sys. Reh. **19**, 325–332 (2011).
6. P. Tathireddy, D. Rakwal, E. Bamberg, and F. Solzbacher, "Fabrication of 3-dimensional silicon microelectrode arrays using micro electro discharge machining for neural applications," in *Proceedings of the International Conference on Solid-State Sensors, Actuators and Microsystems (Transducers)* (IEEE, 2009), pp. 1206–1209.

#168581 - $15.00 USD Received 15 May 2012; revised 8 Aug 2012; accepted 10 Aug 2012; published 24 Aug 2012

7. R. Normann, D. McDonnall, G. Clark, R. Stein, and A. Branner, "Physiological activation of the hind limb muscles of the anesthetized cat using the Utah Slanted Electrode Array," in *Proceedings of IEEE International Joint Conference on Neural Networks* (IEEE, 2005), pp. 3103–3108.
8. J. A. McNulty, "Histology part 6: Neural tissue, http://zoomify.lumc.edu/histonew/neuro/neuro_main.htm" .
9. J. Wells, C. Kao, K. Mariappan, J. Albea, E. D. Jansen, P. Konrad, and A. Mahadevan-Jansen, "Optical stimulation of neural tissue in vivo," Opt. Lett. **30**, 504–506 (2005).
10. J. Wells, C. Kao, P. Konrad, T. Milner, J. Kim, A. Mahadevan-Jansen, and E. D. Jansen, "Biophysical mechanisms of transient optical stimulation of peripheral nerve," Biophys. J. **93**, 2567–2580 (2007).
11. M. G. Shapiro, K. Homma, S. Villarreal, C.-P. Richter, and F. Bezanilla, "Infrared light excites cells by changing their electrical capacitance," Nat. Commun. **3**, 736 (2012).
12. J. Wells, P. Konrad, C. Kao, E. D. Jansen, and A. Mahadevan-Jansen, "Pulsed laser versus electrical energy for peripheral nerve stimulation," J. Neurosci. Methods **163**, 326–337 (2007).
13. J. Wells, C. Kao, E. D. Jansen, P. Konrad, and A. Mahadevan-Jansen, "Application of infrared light for in vivo neural stimulation," J. Biomed. Opt. **10**, 064003 (2005).
14. R. G. McCaughey, C. Chlebicki, and B. J. Wong, "Novel wavelengths for laser nerve stimulation," Lasers Surg. Med. **42**, 69–75 (2010).
15. N. Fried, S. Rais-Bahrami, G. Lagoda, A.-Y. Chuang, L.-M. Su, and A. Burnett, "Identification and imaging of the nerves responsible for erectile function in rat prostate, in vivo, using optical nerve stimulation and optical coherence tomography," IEEE J. Sel. Topics in Quantum Electron. **13**, 1641–1645 (2007).
16. A. Izzo, J. Walsh, E. Jansen, M. Bendett, J. Webb, H. Ralph, and C.-P. Richter, "Optical parameter variability in laser nerve stimulation: A study of pulse duration, repetition rate, and wavelength," IEEE T. Bio-Med. Eng. **54**, 1108–1114 (2007).
17. J. M. Cayce, R. M. Friedman, E. D. Jansen, A. Mahavaden-Jansen, and A. W. Roe, "Pulsed infrared light alters neural activity in rat somatosensory cortex in vivo," Neuroimage **57**, 155–166 (2011).
18. J. Zhang, F. Laiwalla, J. A. Kim, H. Urabe, R. V. Wagenen, Y.-K. Song, B. W. Connors, F. Zhang, K. Deisseroth, and A. V. Nurmikko, "Integrated device for optical stimulation and spatiotemporal electrical recording of neural activity in light-sensitized brain tissue," J. Neural Eng. **6**, 055007 (2009).
19. J. Wang, F. Wagner, D. A. Borton, J. Zhang, I. Ozden, R. D. Burwell, A. V. Nurmikko, R. van Wagenen, I. Diester, and K. Deisseroth, "Integrated device for combined optical neuromodulation and electrical recording for chronic in vivo applications," J. Neural Eng. **9**, 016001 (2012).
20. S. Royer, B. V. Zemelman, M. Barbic, A. Losonczy, G. Buzski, and J. C. Magee, "Multi-array silicon probes with integrated optical fibers: light-assisted perturbation and recording of local neural circuits in the behaving animal." Eur. J. Neurosci. **31**, 2279–2291 (2010).
21. A. V. Kravitz and A. C. Kreitzer, "Optogenetic manipulation of neural circuitry in vivo." Curr. Opin. Neurobiol. **21**, 433–439 (2011).
22. A. V. Kravitz, B. S. Freeze, P. R. L. Parker, K. Kay, M. T. Thwin, K. Deisseroth, and A. C. Kreitzer, "Regulation of parkinsonian motor behaviours by optogenetic control of basal ganglia circuitry," Nature **466**, 622–626 (2010).
23. V. Gradinaru, K. R. Thompson, F. Zhang, M. Mogri, K. Kay, M. B. Schneider, and K. Deisseroth, "Targeting and readout strategies for fast optical neural control in vitro and in vivo." J. Neurosci. **27**, 14231–14238 (2007).
24. A. N. Zorzos, E. S. Boyden, and C. G. Fonstad, "Multiwaveguide implantable probe for light delivery to sets of distributed brain targets," Opt. Lett. **35**, 4133–4135 (2010).
25. T. V. F. Abaya, M. Diwekar, S. Blair, P. Tathireddy, L. Rieth, G. A. Clark, and F. Solzbacher, "Optical characterization of the Utah Slant OptrodeAarray for intrafascicular infrared neural stimulation," Proc. SPIE **8207**, 82075M (2012).
26. G. A. Clark, S. L. Schister, N. M. Ledbetter, D. J. Warren, F. Solzbacher, J. D. Wells, M. D. Keller, S. M. Blair, L. W. Rieth, and P. R. Tathireddy, "Selective, high-optrode-count, artifact-free stimulation with infrared light via intrafascicular Utah Slanted Optrode Arrays," Proc. SPIE **8207**, 82075I (2012).
27. R. Bhandari, S. Negi, L. Rieth, and F. Solzbacher, "Wafer-scale processed, low impedance, neural arrays with varying length microelectrodes," in *International Solid-State Sensors, Actuators and Microsystems Conference (Transducers)* (IEEE, 2009), pp. 1210–1213.
28. R. Bhandari, S. Negi, L. Rieth, and F. Solzbacher, "A wafer-scale etching technique for high aspect ratio implantable mems structures," Sens. Actuators A **162**, 130–136 (2010).
29. M. Bass, C. DeCusatis, G. Li, V. Mahajan, J. Enoch, and E. Stryland, *Handbook of Optics: Optical Properties of Materials, Nonlinear Optics, Quantum Optics* (McGraw-Hill, 2009).
30. V. Tuchin, *Handbook of Optical Biomedical Diagnostics* (SPIE, 2002).
31. D. Mynbaev and L. Scheiner, *Fiber-Optic Communications Technology* (Prentice Hall, 2001).
32. Y.-F. Li and J. W. Y. Lit, "Transmission properties of a multimode optical-fiber taper," J. Opt. Soc. Am. A **2**, 462–468 (1985).
33. S. Tang, L. Wu, F. Li, T. Li, and R. T. Chen, "Compression-molded three-dimensional tapered optical polymeric waveguides for optoelectronic packaging," Proc. SPIE **3005**, 202–211 (1997).
34. Z.-N. Lu, R. Bansal, and P. Cheo, "Radiation losses of tapered dielectric waveguides: a finite difference analysis with ridge waveguide applications," J. Lightwave Technol. **12**, 1373–1377 (1994).

#168581 - $15.00 USD Received 15 May 2012; revised 8 Aug 2012; accepted 10 Aug 2012; published 24 Aug 2012

35. B. K. Garside, T. K. Lim, and J. P. Marton, "Ray trajectories in optical fiber tapered sections," Appl. Opt. **17**, 3670–3674 (1978).
36. R. Deri and E. Kapon, "Low-loss III-V semiconductor optical waveguides," IEEE J. Quantum. Electron. **27**, 626–640 (1991).
37. F. Bahloul, R. Attia, and D. Pagnoux, "Reduction of the overall coupling loss using nonuniform tapered microstructured optical fiber," in *Proceedings of International Conference on Transparent Optical Networks* (IEEE, 2010), pp. 1–4.
38. S.-C. Hung, E.-Z. Liang, and C.-F. Lin, "Silicon waveguide sidewall smoothing by KrF excimer laser reformation," J. Lightwave Technol. **27**, 887–892 (2009).
39. Q. Xia, P. F. Murphy, H. Gao, and S. Y. Chou, "Ultrafast and selective reduction of sidewall roughness in silicon waveguides using self-perfection by liquefaction," Nanotechnology **20**, 345302 (2009).
40. K. K. Lee, D. R. Lim, L. C. Kimerling, J. Shin, and F. Cerrina, "Fabrication of ultralow-loss Si/SiO2 waveguides by roughness reduction," Opt. Lett. **26**, 1888–1890 (2001).
41. D. Sparacin, S. Spector, and L. Kimerling, "Silicon waveguide sidewall smoothing by wet chemical oxidation," J. Lightwave Technol. **23**, 2455–2461 (2005).

1. Introduction

Electrical stimulation of nerves has been demonstrated as a viable means of neuroprosthesis. Peripheral neuroprostheses typically use interfaces with peripheral nerves or muscles to restore motor and sensory functions [1]. Of these interfaces, the Utah Slant Electode Array (USEA) has been shown to provide comprehensive access to multiple independent motoneuron subpopulations and to effect local stimulation with low current levels, even in a long-term implant [2, 3, 4, 5]. These multielectrode arrays are designed to penetrate deeply into neural tissue, for example, to access the different fascicles within the peripheral nerve, as shown in Fig. 1. A typical USEA can reach up to 1.5-mm deep into tissue, but electrodes as long as 9 mm have been machined using alternative fabrication methods [6]. The variable length intrafascicular electrodes facilitate low stimulation threshold and selectivity with a few electrodes targeting a specific muscle [2]. The electrodes are placed in proximity to the target axons and thus bypass the epineurium and perineurium, which act as insulators that make stimulation from around the nerve (e.g., via cuff electrodes) weaker and less selective. In addition, the high-channel count (i.e., 100 electrodes) allows successive recruitment of neurons to evoke maximal fatigue-resistant forces in various muscles [7]; graded activation of several muscles with the USEA for normal multi-joint motions was demonstrated by producing a graceful feline stance with paralyzed hind limbs of the cat [4].

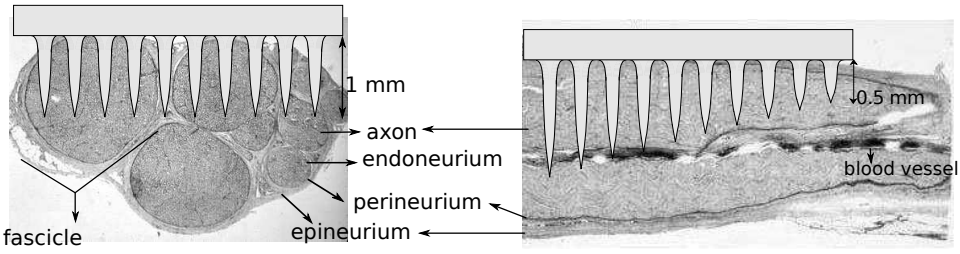

Fig. 1. Utah Slant Electrode/Optrode Array for peripheral nerve stimulation and/or recording. (a) Transverse cross-section of cat sciatic nerve with single row of slant array shown. The microneedles penetrate through epineurium, perineurium and endoneurium to access axons within the fascicle. (b) Longitudinal cross-section showing slant array reaching axons at various depths within the nerve. Adapted from [8].

Electrical signals, on the other hand, cause stimulus artifacts that prevent simultaneous recording and stimulation of adjacent neurons. An alternative modality using infrared light

#168581 - $15.00 USD Received 15 May 2012; revised 8 Aug 2012; accepted 10 Aug 2012; published 24 Aug 2012

as input energy avoids the artifact problem due to the absence of direct charge injection [9]. In the initial study [9], a pulsed IR laser was coupled to a 600-μm diameter optical fiber and the light was incident on a single spot on a rat sciatic nerve surface. Action potentials were selectively evoked without causing histological tissue damage. Stimulation and ablation fluence thresholds were determined for several wavelengths between 2.1 and 6.1 μm. Optimal wavelengths with a safety margin between stimulation and damage threshold for extraneural stimulation of mammalian peripheral nerves was observed to depend on the absorption spectrum of water, the dominant tissue absorber in the IR; damage threshold was strongly affected by the absorption, but stimulation commencement levels varied less. Stimulation at 3 and 6-μm wavelengths, which have very high absorption (i.e., approximately zero penetration depth) as shown in Fig. 2, readily created nerve damage with threshold stimulation fluence; 2.1 and 4-μm wavelengths, which have smaller absorption coefficients, were found to be particularly well suited for infrared neural stimulation (INS). This finding, along with recordings of surface nerve temperatures, suggest that INS acts in nerve via the induction of a spatio-temporal heat gradient in the tissue (4°C at the axonal level) with about 3-mJ/mm^2 extraneural threshold dose [10]. Although the underlying physiological mechanism is still under investigation, the threshold optical dose closely follows the water absorption spectrum. A recent study however, determined that IR is absorbed by water during INS and causes local tissue heating that depolarizes the target cell by changing the membrane electrical capacitance [11].

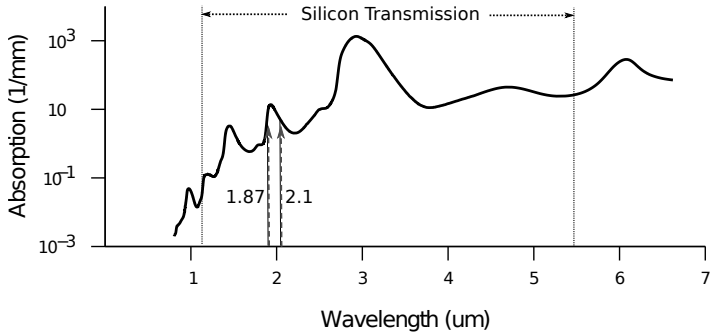

Fig. 2. Water absorption curve for IR wavelengths, which is representative of tissue absorption in the IR. 1.87 μm is recommended for peripheral nerve INS, but 2.1 μm has also been extensively used.

With a 2.12-μm (Ho:YAG laser) input, INS has been demonstrated to achieve a selective excitation volume with respect to extraneural electrical stimulation [12]. A wavelength of 2.12 μm has been extensively used because it causes minimal nerve damage and can be generated from a commercially available Ho:YAG laser that is currently utilized in many clinical applications [9, 13]. This wavelength corresponds to a tissue penetration depth between 300 and 500 μm as supported by Fourier transform infrared spectroscopy results in [12], which is deemed suitable for stimulation based on rat peripheral nerve geometry [13, 12]; a wavelength in the vicinity of 1.87 μm, having similar absorption characteristics as 2.12 μm, has also been shown to stimulate effectively in various applications [14, 15, 16, 17]. However, neural tissue of different types and morphologies may require different wavelengths for optimal stimulation such that the optical penetration depth is matched to the targeted excitable tissue.

As with electrical stimulation, an intrafascicular multiple access approach for INS will likely provide coverage of a large number of independent neuron subpopulations, lower activation energy, and better spatial selectivity than extraneural INS. These advantages may be demonstrated by using *optrode* arrays made from intrinsic silicon (Si), with IR light coupled from a pulsed

#168581 - $15.00 USD Received 15 May 2012; revised 8 Aug 2012; accepted 10 Aug 2012; published 24 Aug 2012

or continuous wave (CW) laser source operating at wavelengths from 1.1 to 5.5 μm, as indicated in Fig. 2. Ultimately, INS with an optrode array is expected to yield a greater separation between stimulation and damage thresholds and permit a wider range of wavelengths to effect a neural response - light does not need to travel through the connective tissues within the nerve in order to reach the axons, potentially allowing wavelengths with high absorption to be used.

Other penetrating probes for optical stimulation have been used in the field of optogenetics, where visible light is delivered to excite genetically targeted neurons expressing light-sensitive channels (e.g., ChR2). Tapered optical fibers serving as tissue-penetrating optical probes have been utilized [18, 19, 20, 21, 22]. A single optrode made of a 50-μm multi-mode fiber was inserted in mouse brain slices to trigger localized epileptiform events in a single cortical site [18]. Simultaneous delivery of visible light to multiple neuronal sites have been achieved by arranging tapered single-mode optical fibers in a 2D array of optrodes [20]; etched fibers were glued to commercially available planar silicon probes, which are an alternative to tungsten electrodes utilized in previous studies [23]. Experiments with ChR2-transfected rat hippocampus demonstrated multiple local stimulation via these 2D arrays. A more sophisticated microfabricated 2D multiwaveguide probe was introduced as an alternative to crude arrays of tapered fibers [24]. The probe targets points along its axis (i.e., stimulation of sites along the depth rather than the lateral direction) using parallel independent single-mode rectangular waveguides of silicon oxynitride core and oxide cladding that converge into a probe structure. Each waveguide ends at a particular target depth with a corner aluminum mirror to perform side-firing; transmission efficiency ranged from 23 to 33% as determined from bench testing.

We have recently developed a micromachined 3D optrode array for infrared neural stimulation. This array covers a wide area of neuronal stimulation sites and reaches targets at varying depths, thereby facilitating high-channel-count optical stimulation. Preliminary optical [25] and *intrafascicular* physiological [26] testing results have been reported. In this paper, we perform detailed characterization of this early-generation Utah Slant Optrode Array (USOA) neural interface. The USOA is designed after the USEA architecture, which has been adapted for numerous physiological requirements, such as nerve dimensions and axon depth, through variation in electrode length and spacing. Note that the same design can be adapted to other transparent substrates for both INS and optogenetic applications.

2. The Utah Slant Optrode Array

The USOA in this paper consists of a 10×10 array of microneedles with lengths varying in one direction from 0.5 mm to 1.5 mm on a 400-μm pitch. Each optrode tapers to a point from a base width of about 180 μm. Fig. 3 is an SEM image of the USOA. Light input to the USOA is provided via optical fibers butt-coupled to the array backside where optrode bases are located. The optrodes act as waveguides and light emitted from the optrode tips stimulates axons in close proximity via local tissue heating.

2.1. Fabrication

Fabrication of the USOA takes advantage of the extensive development of the Utah Slant Electrode Array (USEA) [27]. The arrays are bulk-micromachined from an undoped ($\rho > 20\,\Omega\cdot$ cm) c-Si (100) wafer with 2-mm thickness and 76.2 ± 0.3-mm diameter. This substrate is able to transmit IR at wavelength $\lambda > 1.1\,\mu$m with negligible absorption losses. One wafer yields 49 5×5-mm^2 arrays.

2.1.1. Backside processing

The optical fibers for light input are butt-coupled to a polished side of the Si wafer to minimize any scattering losses. In order to facilitate fiber alignment with the optrode bases, a uniform

#168581 - $15.00 USD Received 15 May 2012; revised 8 Aug 2012; accepted 10 Aug 2012; published 24 Aug 2012

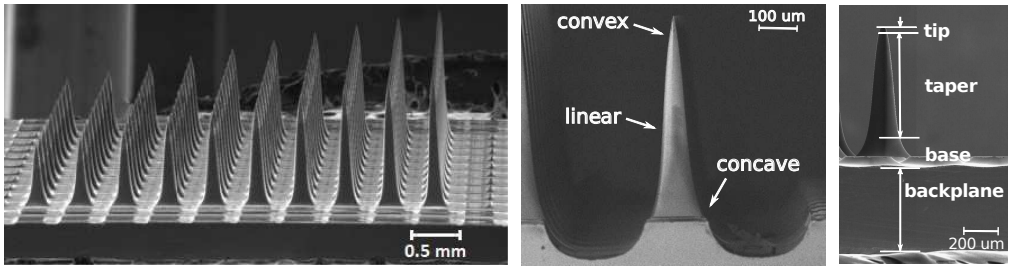

Fig. 3. SEM images of a Utah Slant Optrode Array. The array is bulk-micromachined from intrinsic (100) silicon. (a) Optrode lengths vary from 0.5 to 1.5 mm. (b) Taper profile of the shortest optrode. (c) Definition of optrode sections along the path of light propagation: 500-μm backplane, base extending 120 μm into linearly tapered shank, and $\sim$50-μm tip.

layer of 100-nm Al was deposited with ebeam evaporation on this side and was photolighographically patterned with 10×10 matrices of square windows. These windows were etched into the Al film using aluminum etchant (type A, Transene Co., Inc.). Arrays within the same wafer had different window sizes to accomodate testing with fibers of various core diameters. Part of the backside is shown in Fig. 4, where the windows are $140 \times 140\,\mu\text{m}^2$. This fabrication method is amenable to the integration of an anti-reflection (AR) coating because the AR layer(s) may be deposited before the aluminum.

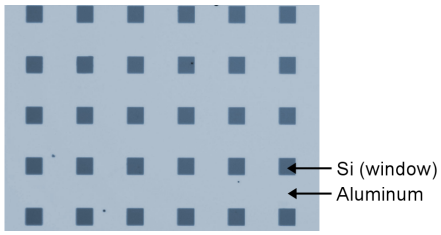

Fig. 4. Optrode backside showing windows in the aluminum layer for fiber alignment

2.1.2. Dicing

A Disco DAD 640 dicing saw was used to form vertical rectangular shanks on the frontside. Fig.5 shows the array transformation during dicing. First, seven sets of twelve cuts of depth gradient from 0.5 mm to 1.5 mm with 0.4-mm spacing are made with a resin blade across the wafer to form a slant in one direction (a). Material in-between the arrays was also removed by dicing before forming the shanks. With a nickel blade, deep kerfs were then diced into the silicon wafer to isolate the varying heights (b), and the same cuts were made in the 90° direction to create pillars (c). Each array had 10 rows of optrodes plus two extra rows on the longest side and three extra rows on the shortest side; in the orthogonal direction, there were two extra rows on each side. The extra rows were sacrifical features designed to enhance uniformity in optrode geometry across the array during wet etching. The average column width after dicing was 240 ± 15 μm.

#168581 - $15.00 USD Received 15 May 2012; revised 8 Aug 2012; accepted 10 Aug 2012; published 24 Aug 2012

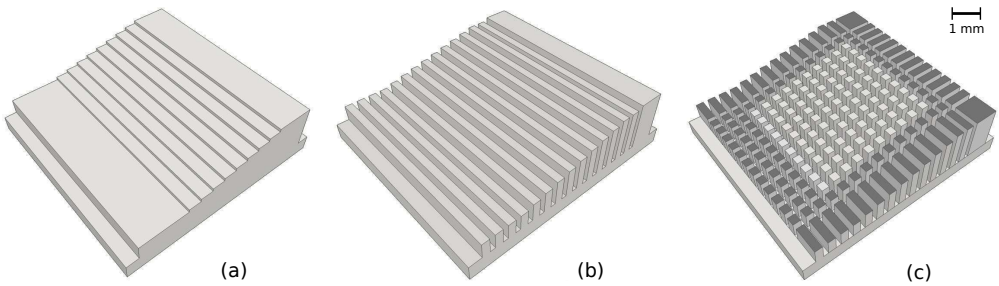

Fig. 5. Array dicing steps. Darker shanks constitute sacrificial regions.

2.1.3. Etching

Wafer-scale etching is a two-step process consisting of dynamic and static etching [28]. Fig. 6 illustrates the principle and Fig. 7 shows the progression of the optrodes during etching. For both steps, the wafer is mounted on a Teflon wafer holder comprised of a top plate and a base plate. The wafer fits into the recess in the base plate, and an O-ring along the edges protects the backside of the wafer from the wet etchant. The top plate is a donut-shaped piece that screws on the base plate and acts as a frame to secure the wafer in place.

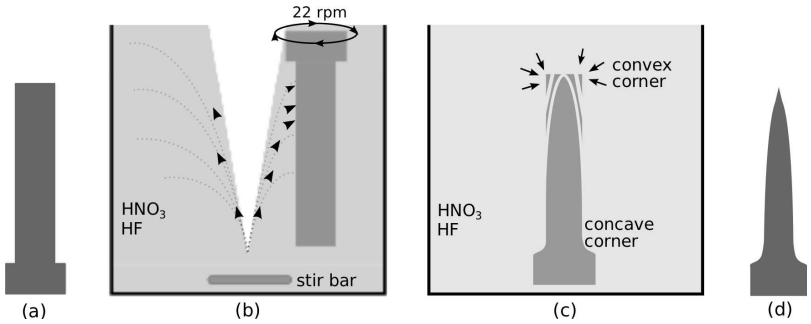

Fig. 6. Etching steps. (a) Initial shape of shanks. (b) Dynamic etching is performed for isotropic thinning. (c) Static etching preferentially sharpens the tips. (d) A missile-shaped optrode is formed. The arrows indicate locations of pronounced etching.

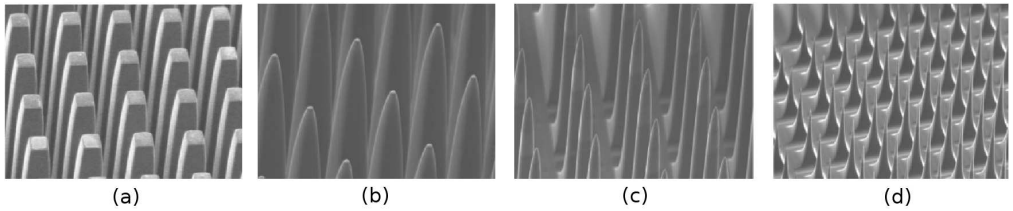

Fig. 7. SEM images showing optrode shape at different stages of the etching process. Dynamic etching narrows the shank (a), while static etching sharpens it (b-d). As etch time progresses, the tips progress from being blunt (b) to missile-shaped (c) to over-etched (d).

During dynamic etching, the wafer is immersed with columns facing down into 1500 ml of 1:19 acid mixture of HF (49%) and HNO_3 (69%). The wafer is rotated clockwise (22 rpm),

#168581 - $15.00 USD Received 15 May 2012; revised 8 Aug 2012; accepted 10 Aug 2012; published 24 Aug 2012

while a magnetic stirrer in the solution rotates counter-clockwise (500 rpm) to cause an aggressive and continuous flow of etchant into the high aspect ratio columns. This leads to uniform etching across the side-walls of the square columns. Apart from the rotation speed, other important dynamic etching parameters are the separation between the magnetic stir-bar and wafer (2 in), temperature of the etching solution (room temperature, but slightly increased because of exothermic etching reaction) and the etch time (5 min).

In static etching, the holder is placed in 750 ml of fresh acid mixture with the columns facing upwards. The diffusion-limited reaction and the relative inactivity at the base of the shanks preferentially etches the top of the columns until a sharp tip is formed. To ensure uniform static etching, a pipette is used to continuously remove byproducts near the top surface and circulate the solution. Static etch time is approximately 5 mins, which is when the optrodes are missile-shaped. Beyond this time, the optrodes become thinner.

2.1.4. Singulation

The last step is to separate the individual arrays from the wafer. A nickel blade was used in the dicing saw to trim the arrays into 10×10 structures by cutting off the sacrificial rows. Then, a resin blade was used to pierce the backside for singulation. The array in Fig. 3 is finally formed.

3. Theoretical loss mechanisms

The geometry of the optrodes and its input and output interfaces dominate the losses in the system. The primary loss mechanisms are expected to be Fresnel reflections (R), mode coupling, radiation, and loss due to reflection towards the source. Fig. 8 shows where these losses occur. The power from the fiber P_{in} is reduced by the transmittance $T_{\mathrm{i}} = (1 - R_{\mathrm{i}})$ to P'_{in}, which is the power introduced to the Si backplane. P_{back}, P_{base} and P_{shank} are radiation losses, while P_{ref} is the lumped reflection loss from all sections within the device; absorption loss is assumed negligible. The output from the optrode tip is P_{out}. Power coupled into the shank and the power entering the tip is represented by $P_{coupled}$ and P_{tip}, respectively. The variables are related through

$$P_{in} \times (1 - R_{\mathrm{i}}) = P'_{in} = P_{back} + P_{base} + P_{shank} + P_{out} + P_{ref}.$$

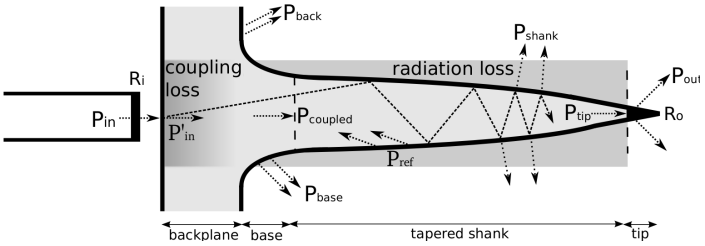

Fig. 8. Loss mechanisms within the optrode include Fresnel reflectance ($R_{i/o}$), coupling, radiation and backreflection losses.

3.1. *Fresnel reflections*

Fresnel reflection loss will occur at both the optrode backside and tip, which are the fiber-to-Si and Si-to-tissue interfaces, respectively. Table 1 lists the refractive indices (n) under consideration, while Table 2 shows relevant reflectance values as computed from

$$R = \left(\frac{n_1 - n_2}{n_1 + n_2} \right)^2, \tag{1}$$

#168581 - $15.00 USD Received 15 May 2012; revised 8 Aug 2012; accepted 10 Aug 2012; published 24 Aug 2012

for a single interface, where n_1 and n_2 are the refractive indices of the materials on either side of the interface. For double interfaces, as in the gap between the fiber and Si backside, this equation is applied twice, using the relation

$$R_{\text{eff}} = 1-(1-R_1)(1-R_2) = R_1+R_2-R_1R_2.$$

Note that interference effects were not considered.

Table 1. Refractive indices at 1.55 μm

Material	n	Reference
Air	1.00	
Silicon	3.48	[29]
Fused Silica (Fiber)	1.44	[29]
Tissue	1.36	[30]

Table 2. Reflectance at interfaces

Interface	Reflectance (R)	Transmittance (1-R)
Fiber-Air-Si	0.329	0.671
Fiber-1.44-Si	0.172	0.828
Fiber-1.66-Si	0.130	0.870
Si-Tissue	0.192	0.808
Si-Air	0.306	0.694

A fiber in contact with bare silicon leaves an air gap junction, which has an overall Fresnel reflectance loss of 32.9%. This gap can effectively be eliminated by using index matching fluid ($n = 1.44$), with index that matches that of the fiber; nevertheless, the remaining single-interface drops reflectance to 17.2%, leaving a theoretical maximum of 82.8% that can be transmitted to tissue. Using a higher refractive index fluid in the gap, such as $n = 1.66$, further reduces the reflectance loss to $\sim$13%. In principle, an anti-reflection (AR) coating could be designed to minimize reflection loss at the input interface, but fiber index matching fluid would still be used to fill-in the air gap.

3.2. Mode coupling

Due to its high refractive index, the Si optrode is highly multi-moded. Losses in the coupling between two multi-mode waveguides are described in most textbooks on fiber optics [31], and are geometrical in nature. Extrinsic losses are due to alignment, including lateral displacement and end separation.

The intrinsic losses are due to mismatches in the core cross-sectional area (A) and numerical aperture (NA) between the fiber and optrode. The coupling efficiency (η) resulting from these losses may be quantified as

$$\eta_A = \frac{A_O}{A_F} \tag{2}$$

and

$$\eta_{\text{NA}} = \left(\frac{\text{NA}_\text{O}}{\text{NA}_\text{F}}\right)^2, \tag{3}$$

#168581 - $15.00 USD Received 15 May 2012; revised 8 Aug 2012; accepted 10 Aug 2012; published 24 Aug 2012

where the subscripts O and F signify the optrode and fiber waveguides, respectively. The effective numerical aperture of a tapered waveguide (for meridional rays) is given by

$$\mathrm{NA} = \frac{d_{min}}{d_{max}} cos\theta \sqrt{n_1^2 - n_2^2}, \tag{4}$$

where d_{max} and d_{min} are the diameters of the larger and smaller ends of the taper, n_1 and n_2 are the core and cladding indices, and θ is the angle of the taper slope with respect to the propagation direction [32].

Although the use of lensed fibers or external lenses may increase coupling efficiency, our studies were performed by direct fiber to optrode coupling for simplicity. Given the large refractive index contrast of the optrodes and the relatively small coupling fiber NA, we don't expect NA mismatch to be a significant source of loss.

3.3. Radiation and scattering loss

Radiation loss for the optrode is expected to result from its taper; higher-order guided modes are transformed into radiation modes as the diameter of the optrode decreases along its length. A simplified mathematical relationship that provides insight on how taper affects waveguide efficiency has been derived for a multi-mode to single-mode tapered slab using coupled-mode theory [33, 34]

$$P_{rad} = \left(\frac{3n}{8\pi} \frac{d_{max}^2 - d_{min}^2}{\lambda z} \right)^2, \tag{5}$$

where P_{rad} is the power loss normalized by the input power, n is the waveguide effective refractive index, λ is the wavelength, z is the propagation distance, and d_{max} and d_{min} are the maximum and minimum taper diameters, respectively. It is clear that more tapered waveguides (i.e., higher taper slope or angle) suffer from higher radiation loss. This is consistent with ray optics, from which it has been shown that higher taper slopes result in fewer total internal reflection (TIR) points along the waveguide wall and thus leak more power out as radiation [35]. It has been further shown that it is the higher order modes that significantly contribute to the loss [34], which correspond to the larger ray angles.

Likewise, 2D conical waveguides are expected to lose more power with increasing taper slope. Analysis on ray trajectories in multi-mode cylindrical linearly tapered optical fibers reveals that the total light transmitted from both meridional and skew rays is quadratically proportional to the effective numerical aperture of the taper (Eq. 4) [32]. Large diameter and high refractive index contrast silicon waveguides, such as the optrodes, are highly multi-moded and require extensive ray tracing analysis for accurate prediction of taper loss, but we will make use of Eq. 5 to provide qualitative insight.

Light may also be scattered inside the optrode when the guided modes interact with the etched waveguide surface. Scattering due to surface roughness is exacerbated by high refractive index contrast. For instance, the scattering loss for a symmetric slab waveguide with core index n_1 and cladding index n_2 has been modeled as [36]

$$P_s = \frac{\sigma^2 k_0^2 h}{\beta} (n_1^2 - n_2^2) E_S^2, \tag{6}$$

where σ is the roughness, k_0 is the free space wavenumber, h is transverse propagation constant in the cladding, β is the mode propagation constant and E_S is the normalized electric field amplitude at the core-cladding interface. Furthermore, light scattering may be more significant from an optrode in tissue due to the inherent inhomogeneity of tissue.

#168581 - $15.00 USD Received 15 May 2012; revised 8 Aug 2012; accepted 10 Aug 2012; published 24 Aug 2012

4. Characterization results and discussion

In all experiments, the optrode arrays were tested in air with a bare fiber mechanically aligned to one aluminum window on the backside at a time; the fiber was in contact with, but not attached to, the optrode base. Multiple measurement conditions were used to assist in separating the losses from the different regions of the optrode, as indicated in Fig 9. To isolate the output power, the optrode tips were punched through a thin aluminum foil (producing a 10×10 matrix of holes) in order to expose only the last 50 μm of each optrode to block light radiation from anywhere else along the propagation path (a); an IR detector was used to compare the light transmitted through the tip with the light transmitted through the coupling fiber. The optrodes were also inserted all the way through until the foil rests against the backplane in order to collect taper loss (b). Light leaking through the base region, which extends 120 μm from the backplane, was measured by covering only the backplane area between the optrodes using a 50-μm thick aluminum plate with pre-drilled holes that are 300 μm in diameter (c). Backplane radiation was included in the measurements by exposing all sections of the optrode (d). All radiation data were determined with an IR integrating sphere that captures light transmitted through the device at large angles, with the results normalized to the fiber output also measured with the integrating sphere. A 1550-nm continuous wave input is used for all measurements, except as noted with the Capella laser. A wavelength within the telecommunications band was used because of the availability of instrumentation that operates in this band. Telecommunications wavelengths have been demonstrated effective for INS [14].

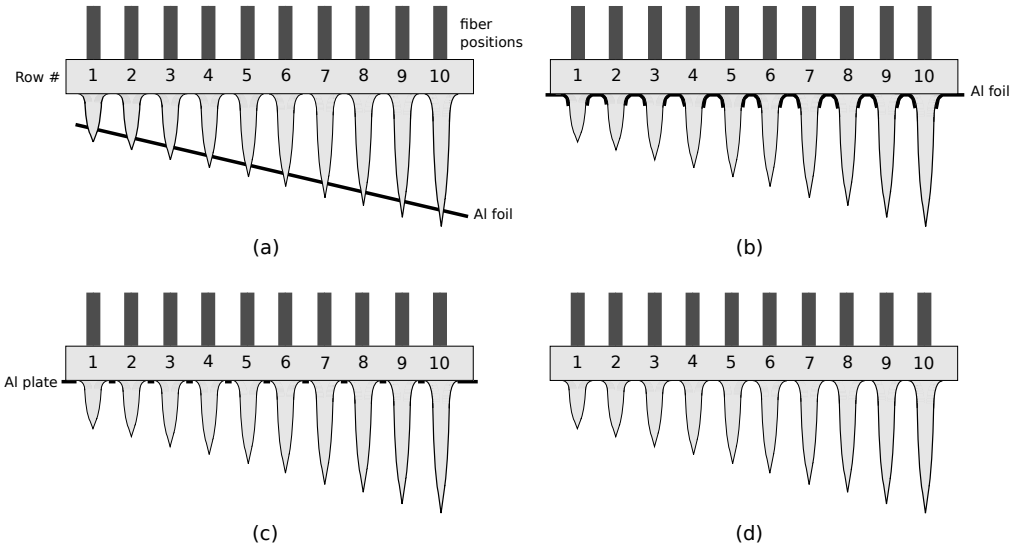

Fig. 9. Experimental setup. (a) Measuring output power from optrode tips. (b) Measuring taper loss from the shank. (c) Measuring base radiation. (d) Measuring backplane radiation.

4.1. Accounting for the backplane Fresnel loss

To verify the contribution of Fresnel reflection (R) at the input to the overall loss, the refractive index of the fiber to Si gap was varied ($n = 1.66, 1.44, 1.0$) with the use of index matching fluids. A 50-μm fiber with 0.22 NA delivered light to the optrode in these three sets of measurements. Light out of each optrode tip was collected by an IR photodetector. The fraction of power transmitted from fiber tip to optrode tip is shown in Fig 10(a). The three lines correspond to the different refractive indices used. The data points are plotted against the rows in the slant

#168581 - $15.00 USD Received 15 May 2012; revised 8 Aug 2012; accepted 10 Aug 2012; published 24 Aug 2012

array, which are aligned to the actual optrode length scale above the graph; Row 10 contains the longest optrodes as labeled in Fig. 9. The variation of the transmittance with optrode length is discussed in the next section.

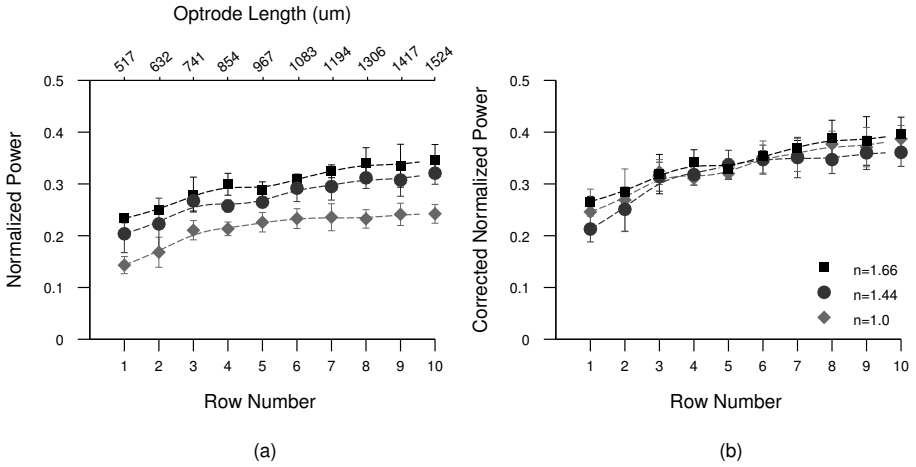

Fig. 10. Normalized output power from optrode tips with varying refractive index at the input interface using a 50-μm fiber with 0.22 NA.

The theoretical reflectance losses at the input with $n = 1.66$, $n = 1.44$ and air ($n = 1.0$) interfaces are 0.130, 0.172 and 0.329, respectively, resulting in an input transmittance value of $T_{\mathrm{i}} = 0.87$ for the $n = 1.66$ interface. Without the input reflectance, the transmitted power for all cases should be equal because the remaining losses depend only on the fiber and optrode geometries. The output values, removing the input reflectance loss, are plotted in Figure 10(b). The line plots overlap within error, thus confirming the contribution of backside reflection loss as an independent factor. Note that if an AR coating were applied on the backside, the maximum efficiency attained would be about 39%, suggesting that it is more beneficial to reduce the remaining loss mechanisms.

4.2. Identifying other loss mechanisms

In order to assess the remaining loss mechanisms, transmission measurements from multi-mode fibers of different core sizes were performed. Fibers with 0.22 NA with diameters 50, 105, 200 and 400 μm were used to couple light to the optrodes through an n=1.66 medium. To separate the backplane reflection from all other sources of loss, T_i is factored out from all subsequent data; the resulting values are equivalent to the normalized output power with respect to the amount of power entering the device P'_{in}. Fig. 11(a) and (b) show normalized measurements for the different optrode lengths by coupling with 50 and 105-μm fibers, respectively. The lowest curve is the transmittance through the optrode tips, measured as before using the aluminum foil to block all other radiated light. The upper curve represents all of the light that passes through the USOA device (i.e., all of the light that does not reflect back towards the source or that is waveguided within the backplane). The same line plot is also the light measured by the sphere when the backplane is blocked with the aluminum plate. The middle curve is measured after further covering the base region. The set of curves reveal that the difference in the output power across different optrode lengths results from the varying taper slope; this is not surprising since the backplane and base geometry is the same for all optrodes. Note that these results will vary slightly when the optrode is applied *in vivo*, as the receiveing medium will go from $n = 1$ to $n = 1.34$ (i.e., tissue); the associated critical angle will increase and the

#168581 - $15.00 USD Received 15 May 2012; revised 8 Aug 2012; accepted 10 Aug 2012; published 24 Aug 2012

reflectance will decrease, both of which may allow higher transmission through the tips. Ray tracing simulations verify that the output power increases in a higher index medium.

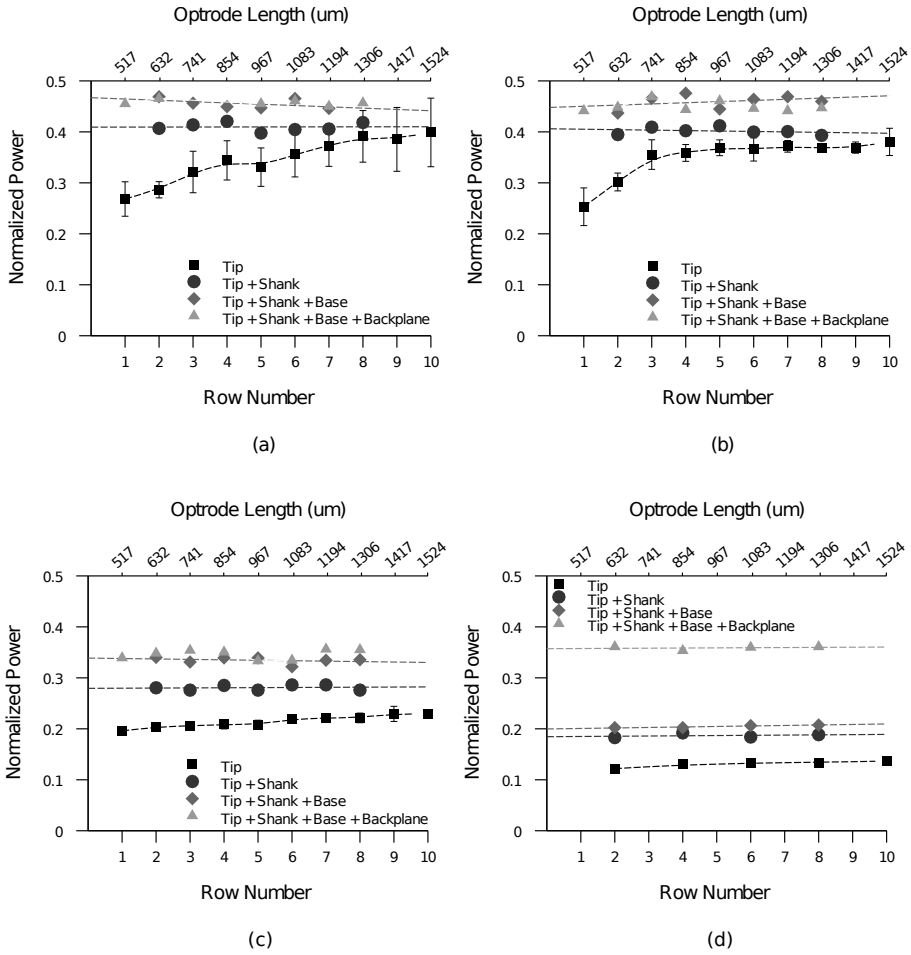

Fig. 11. Measurements to isolate coupling and taper losses with T_i factored out. Normalized tip output and radiation measurements from integrating sphere are shown. Fibers of 0.22 NA with 50-μm (a), 105-μm (b), 200-μm (c) and 400-μm (d) core diameters are coupled to the input.

The same measurements coupling from 200 and 400-μm optical fibers are shown in Fig. 11(c) and (d). Note that because the optrode pitch is 400 μm, alignment windows for the 400-μm fiber were placed only on even rows. In the case of the 400-μm fiber, there are two distinct upper curves, which signify that light is transmitted through the backplane.

The amount of power leaking through the backplane is largely due to the mismatch between the beam spot size and the base area; the NA mismatch between the fiber and optrode is not expected to represent a significant source of loss because $\mathrm{NA}_F < \mathrm{NA}_O$. The beam diameter at the optrode base is widened within the USOA backplane because of the NA of the fiber. Beam profiles of the coupling fibers were determined (section 4.3) and with the 0.5-mm backplane thickness, the effective beam sizes (i.e., width at $1/e^2$ of peak power) at the optrode base are estimated to be 89, 132, 253, and 433 μm for the 50, 105, 200, and 400-μm diameter fibers. Because the optrode base width is about 300 μm, we expect only light from the 400-μm fiber to

#168581 - $15.00 USD Received 15 May 2012; revised 8 Aug 2012; accepted 10 Aug 2012; published 24 Aug 2012

transmit through the backplane. The backplane radiation, which is derived from the difference between the *Tip+Shank+Base+Backplane* and *Tip+Shank+Base* curves of Fig. 11, supports this hypothesis as negligible backplane radiation is observed for fibers smaller than 400 μm. From the area mismatch (Eq. 2), 52% of the beam power from the 400-μm fiber will not be coupled into the base. Only 17% of the power falling outside the base region is measured as radiation, where 35% is expected otherwise. With the concaved backplane surface between the optrodes and the beam size larger than the pitch, rays outside of the base are likely to strike a curvature, undergo TIR and further backreflect towards the source.

Next, the loss due to base radiation is taken from the the difference of the *Tip+Shank+Base* and *Tip+Shank*, which is about 5% except for a 400-μm fiber. For the 400-μm fiber however, upon considering that only 48% of the power is coupled into the base according to previous theoretical analysis, the fractional base radiation loss with respect to the power entering the base is close to 5% as well. The base, like the shank and tip regions, is tapered. Fig. 3 shows the change in the optrode taper from a highly concave shape at the base to convex near the tip; from the effective aperture area above the base up to just below the tip, the optrode tapers linearly. These tapered regions reduce the overall transmission due to radiation and reflection losses. Radiation losses result from rays that don't satisfy TIR conditions, while rays that propagate at steep angles with respect to the optical axis can reflect back towards the source. The base is expected to act as a bottleneck for transmission since highly concave tapered waveguides have been found to exhibit higher propagation loss based on numerical studies [37]; in the case of the optrodes, the small input beams and the short base section prevents the huge loss. In theory, the 50 and 100-μm fibers should not incur base radiation as the optrode width into the shank is still larger than the beam size. However, even a few microns input misalignment will cause the small measured radiation. For bigger fibers with rays striking the base, the number of TIR reflections is decreased as propagation continues in the shank. A collimated input beam may be directed into the optrode shank in order to reduce the losses.

Shank loss depends on optrode length. Shanks inherently have different taper shapes and angle because optrodes of different lengths essentially have the same base shape and taper to about the same diameter at the tip. Shorter optrodes then result in a larger taper angle with respect to the propagation direction. This consequence is discernible in Fig. 3. Transmission through the shank, which is reduced primarily due to radiation loss, can be quantified and compared with theory. The steeper taper of the shorter optrodes causes more power loss, as briefly discussed in section 3.3. This is supported by the difference between the *Tip+Shank* and *Tip* curves of Fig. 11, which estimates the fraction of P'_{in} is radiated out of the optrode shanks. Results with larger input fibers exhibit greater loss and less variation with optrode length because most of the rays that have been directed into the shank have smaller angles with respect to the optical axis.

In order to compare the results with the simple coupled mode theory (CMT) approximation in Eq. 5, which is normalized to the power entering the taper (i.e., $P_{coupled}$), the CMT equation is fitted to the measured data with a single normalization factor. In this way, the loss trend is readily apparent. The matched data are plotted in Fig. 12. CMT predicts the change in radiation loss with varying taper slope for the smaller coupling fibers. Note that the CMT estimate is derived for a multi-mode to single-mode slab and accurate for low index contrast waveguide, whereas optrodes are highly multi-moded high index contrast 3D waveguides. Thus, with the data-fitting, the results presented in Fig. 12 reflect the slope to which the radiation is affected by the taper rather than the comparison between actual and theoretical radiation loss; although 3D waveguides are typically approximated as slabs, CMT underestimates the loss in multimode-to-multimode waveguides [34] and has its limitations when applied to high index contrast interfaces.

#168581 - $15.00 USD Received 15 May 2012; revised 8 Aug 2012; accepted 10 Aug 2012; published 24 Aug 2012

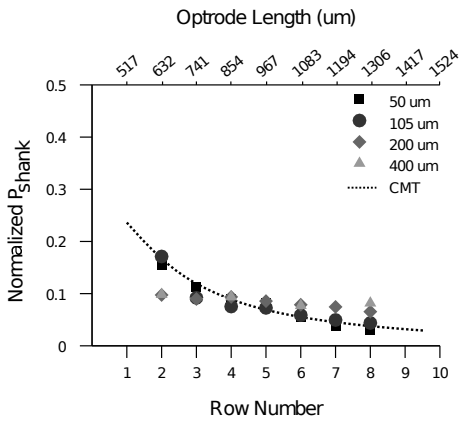

Fig. 12. Radiation loss through the tapered shank after factoring out T_i and fitting the CMT estimate. Fibers of 0.22 NA with varying core diameters are coupled to the input.

Scattering of light inside the shank due to sidewall roughness was considered. The surface roughness of the etched optrode walls was measured using atomic force microscopy (AFM) with an angled tip; the RMS roughness is determined to be 4.4 nm, which is considered optically smooth when compared with previously published results on silicon waveguides. Nevertheless, surface roughness may further be reduced by sidewall smoothing techniques. Lasers (e.g., KrF and XeCl excimer) have been used to decrease roughness via surface reflow in ridge waveguides; the laser selectively melts the sidewall edge, which flows under surface tension and solidifies into a smooth rounded layer [38, 39]. Creating a blanket layer of oxide (e.g., by wet oxidation) over the waveguide and subsequently etching it has also been proven to lower surface roughness [40]. For the high-contrast optrode, repeated wet oxidation and etching is perhaps the most practical approach [41].

The loss unaccounted for by the measurement results (i.e., $\sim 54\%$) is taken as the lump sum of reflection losses P_{ref} from all sections of the optrode. From the results and previous discussion, it is estimated that reflection losses at the tip dominate the system loss; this includes both the Fresnel reflectance on transmitted rays and rays that undergo two TIR's and are completely backreflected. P_{ref} for the smaller fibers is mainly due to reflection at the tips, whereas reflection from the base and backplane is included with values for the larger fibers.

4.3. Beam profiling

Beam profiling was performed to measure the effective spot size and divergence of the light exiting the optrode tips. Table 3 shows values of the beam width ($2W_0$) calculated at 13.5% ($1/e^2$) of the peak power at the optrode tip for different lengths, while Table 4 lists the far-field full divergence angle (ϕ). The measurements were made with 0.22 NA fibers of different core sizes at the input side without any index matching fluid.

The optrode output beam exhibits an approximate gaussian profile (1.56 M^2 fit on average) similar to that in Fig. 13; M^2 fit values of the profiles are also listed, in parentheses, in Table 3. Precise values of the beam width across different rows for the same input fiber were measured. For increasing fiber diameter, it appears that the beam width increases as well. However, values for the 200-μm fiber seem anomalous, which might be an effect of the higher divergence of this particular fiber as measured from the beam profiler.

The beam divergence depends on the divergence of the input fiber as well. More importantly, it varies with the optrode length/taper; the beam diverges more from the more tapered shorter

#168581 - $15.00 USD Received 15 May 2012; revised 8 Aug 2012; accepted 10 Aug 2012; published 24 Aug 2012

Table 3. Beam width ($2W_0$) in μm at 13.5% of peak power and M^2 fit.

Fiber Core Diameter (μm)	Fiber $2W_0$	Optrode $2W_0$ (M^2)		
		Row 4	Row 6	Row 8
50	41.4	46.3 (1.33)	44.0 (1.11)	45.2 (1.28)
105	71.9	51.7 (1.52)	54.7 (1.92)	50.2 (1.54)
200	188.0	71.4 (2.60)	63.2 (1.56)	66.2 (1.25)
400	378.0	66.8 (1.34)	65.4 (1.80)	61.7 (1.51)

Table 4. Beam far-field full divergence angle (ϕ) in $^\circ$ and Rayleigh distance (z_R) in μm.

Fiber Core Diameter (μm)	Fiber ϕ	Optrode ϕ (z_R)		
		Row 4	Row 6	Row 8
50	18.9	16.3 (163)	14.5 (174)	14.0 (185)
105	23.9	17.9 (165)	16.8 (187)	14.2 (202)
200	26.1	20.1 (204)	19.7 (184)	15.7 (241)
400	22.1	17.8 (215)	14.7 (255)	13.6 (260)

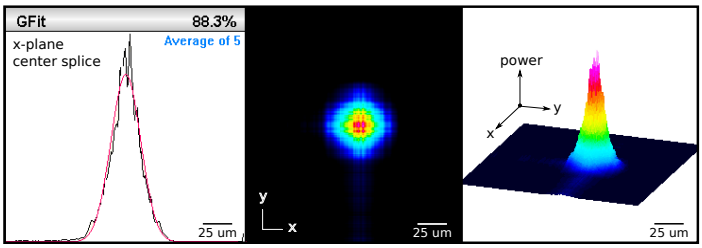

Fig. 13. Beam profile of a Row 6 optrode with a 105-μm input fiber of 0.22 NA. Power is relative to peak; widths vary according to row number and input fiber size.

optrodes. This observation may be explained using simple ray tracing analysis, as illustrated in Fig. 14, which is also supported by wave optics [35]. As light travels down the taper, its propagation angle θ_z increases after each wall reflection. This creates a smaller angle of incidence θ_i at the core-cladding interface that eventually loses total internal reflection. Because the taper angle ω is larger for shorter optrodes, θ_z increases more rapidly and rays exit away farther from the tips, which leads to a wider beam divergence.

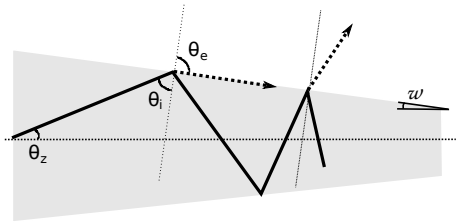

Fig. 14. Ray trajectory in a tapered waveguide. Because there is a faster increase in the propagation angle of a ray travelling through shorter optrodes, the rays exit away farther from the tip, which leads to a wider beam divergence.

The spatial divergence profile of the beam from an optrode in Row 6 with a 105-μm input

#168581 - $15.00 USD Received 15 May 2012; revised 8 Aug 2012; accepted 10 Aug 2012; published 24 Aug 2012

fiber is shown in Fig. 15; the beam width is plotted against the propagation distance along the z-plane. The plot is generated by using an M-squared fit for the beam width curve from measurement points of the beam profiler. The beam waist at the tip (i.e., 0 mm position) is 54.7 μm and broadens to 297.6 μm at a distance 1 mm away. Another important parameter in the *z*-profile is the Rayleigh distance (z_R), which defines the volume of effective energy deposition within the receiving medium. The Rayleigh distance defines how far the beam can travel before expanding considerably, beyond which the full angle divergence is measured; it is distance along the propagation direction where the minimum beam width increases by a factor of $\sqrt{2}$. The beam does not immediately diverge out from the optrode tip and is rather focused, but its energy quickly spreads beyond z_R. In Fig. 15, the beam energy extends 187 μm from the tip into the medium without significant divergence. Table 4 lists z_R for all beams; less divergent beams have a greater focus depth.

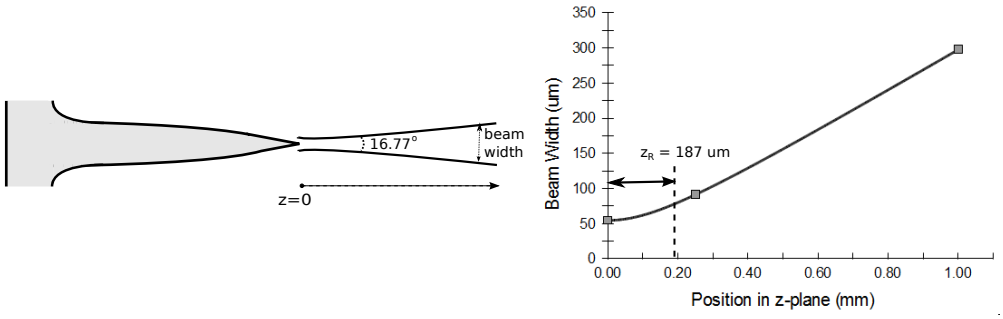

Fig. 15. Changes in beam width with propagation distance from an optrode in Row 6 of the array with a 105-μm input fiber of 0.22 NA.

The output beam divergence and width is predicted to decrease *in vivo* because of the higher refractive index of tissue; this is confirmed by ray tracing simulation results.

4.4. Coupling with the Capella laser

For physiological testing, a Capella laser (Aculight Corporation Infrared Neural Stimulator), with a pulsed output in the wavelength range of 1865 – 1879 nm, is used [26]. Thus, it is important to compile transmission characteristics from the Capella as well. Output power for all measurements were collected using a thermopile sensor. The wavelength chosen for the tests is 1875 nm, pulsed at 10 Hz with a duration of 17 μs to allow the use of the Coherent LabMax-TOP power meter.

4.4.1. Coupling efficiency from laser to fiber

The Capella laser has a ~400-μm emission aperture. A 400-μm fiber is then expected to collect a large fraction of light emitted by the laser. Halving the fiber core diameter is expected to reduce the output power from the fiber to one-fourth as the effective collecting area decreases by the same amount. Table 5 lists the power coupled from the Capella to multi-mode fibers of different diameters. Notice that the output power is about 25% of the value in the next row (i.e., when the core diameter is doubled), which is in accord with expectation.

4.4.2. Coupling efficiency from fiber to optrode

The 200 and 400-μm fibers were used to couple the laser to an optrode with an $n = 1.66$ gap interface. The percentage transmission is shown in Fig. 16 for both fibers across all rows. Note that the trend is consistent with the results in section 4.2, but with slightly lower values. The

#168581 - $15.00 USD Received 15 May 2012; revised 8 Aug 2012; accepted 10 Aug 2012; published 24 Aug 2012

Table 5. Transmitted power from the Capella laser to multi-mode fibers of different diameters

Core Diameter (μm)	Input Power (W)	Output Power (W)	Transmittance (%)
100	5	0.30	6.0
200	5	1.28	25.6
400	5	4.70	94.0

$<$ 2% decrease between the 1550 to 1875 nm results may possibly be due to a difference in the distribution of modes in the multi-mode fibers. The laser source at 1550 nm is single mode, while the Capella is multi-moded, so launching conditions at the input are different. Moreover, we used short ($\sim$1 m) lengths of optical fiber, which are likely shorter than the equilibrium length, which is the length at which the power distribution across the modes stops changing. The slight discrepancy in the results might also simply be due to variations in the measurement setup; a pyroelectric sensor with a 10-mm wide aperture was used; the optrode shanks were positioned normal to the active area by resting the array on a frame atop the detector. The distance between an optrode tip and the detector depends on the optrode length, but reference measurements reveal that there is only about 0.25% decrease in the power detected for a 1-mm increase in the distance.

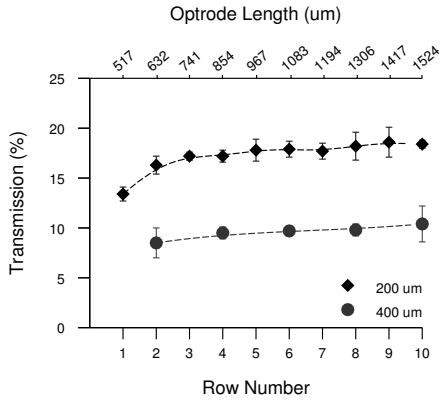

Fig. 16. Transmission through the optrode tips with 200 and 400-μm fibers using the Capella laser (1875 nm). The input coupling interface has n=1.66.

4.4.3. Overall system efficiency

The efficiency of the entire stimulation system for physiological experiments is computed by multiplying the results in sections 4.4.1 and 4.4.2. Table 6 shows a breakdown of the system efficiency and the output power expected to be delivered by the longest optrodes when the Capella emits 5 W. The maximum transmission is obtained using a 400-μm fiber. However, the overall efficiency is only 9.6%, producing 0.48 W of power from the optrode tips.

5. Improving the USOA efficiency

The efficiency of the USOA may be increased with techniques as outlined in Table 7. The table also summarizes the relevant losses determined from bench testing in air, as discussed throughout the paper, and the predicted loss after it is minimized. Fresnel reflection is taken as the theoretical value, while taper, base and backplane losses are computed from measurement

#168581 - $15.00 USD Received 15 May 2012; revised 8 Aug 2012; accepted 10 Aug 2012; published 24 Aug 2012

Table 6. Total efficiency (%) of coupling light from the Capella to the longest optrodes with varying fiber core sizes. Output power from the optrode tips is listed for a Capella emitting 5 W. For the 105-μm fiber, the overall efficiency and output power are estimated at $\lambda = 1550nm$.

Core Diameter (μm)	Laser-Fiber Efficiency	Optrode Efficiency at 1875 (1550) nm	Overall Efficiency	Output Power (mW)
100	6	— (33.0)	(1.98)	(99)
200	25.6	18.2 (20.0)	4.66	233
400	94	10.2 (11.8)	9.59	480

results from the integrating sphere with respect to the power entering the silicon. Antireflective coatings will eliminate the input and output Fresnel losses, while better in-coupling via lenses to collimate or focus the light into the effective aperture of the shank will reduce the backplane and base losses; note that the use of single-mode coupling fibers would in principle allow better control over the input beam properties. Taper losses and TIR within the tips may be reduced with more efficient shank and tip design, although there may be tradeoffs between optical performance and probe insertion properties. Ray tracing simulations will aid in studying alternative tip shapes. With tip losses minimized only by means of an AR layer and assuming the worst case improvement by taking a 31% Fresnel reflectance at the tip interface (i.e., Si-Air), the total laser to optrode transmission efficiency may be improved to a maximum of 64% given a laser source with aperture of $\leq 100\,\mu$m.

Table 7. Expected normalized power loss of the longest optrode when using a 50-μm input fiber with loss-minimization techniques. Optimizing tip shape is not yet considered.

	Current Loss	Solution	Expected Loss
Input interface	0.13	AR coating	$\sim$0
Backplane radiation	$\sim$0	focus/collimate	~ 0
Base radiation	0.05	focus/collimate	$\sim$0
Taper radiation	0.03	remove taper	$\sim$0
Tip losses	0.54	AR coating	0.36
Total	**0.62**		**0.36**

6. Conclusion

A neural interface for deep-tissue IR stimulation has been designed and tested. The Utah Slant Optrode Array, consisting of 10×10 varying length microneedle waveguides, was fabricated based on electrode array processing with key features altered to facilitate light transmission instead. Output power was measured from the optrode tips under various settings to characterize transmission efficiency; the optrodes exhibited losses from Fresnel reflection, mode coupling, radiation due to the tapered geometry and total internal reflection in the tips. Fresnel loss at the in-coupling interface contributed an independent reduction in transmittance, which is small compared to other loss mechanisms. Only coupling loss from a 400-μm fiber is significant, but light interactions with the base sidewall from using larger fibers cause more taper losses. Taper losses increased with shorter optrodes in accordance to the CMT model. Scattering loss is included in taper loss, but is deemed insignificant. In addition to the output power measurements, the effect of the optrode taper on the loss was established with beam profiling, where it was evident that power loss and divergence is greater for shorter, more tapered optrodes. With a

#168581 - $15.00 USD Received 15 May 2012; revised 8 Aug 2012; accepted 10 Aug 2012; published 24 Aug 2012

100-μm fiber delivering 1550-nm light to the optrode, the beam width at the tip is about 55 μm and diverges in the far-field at a full angle of 17°. The majority of the system loss for smaller input fibers is attributed to tip losses, which includes both Fresnel and total internal reflection.

Similar tests were performed with more direct relevance to physiological studies using the Capella laser. The coupling losses from the laser to fibers of smaller than 400-μm diameter dominate the overall system loss, overcoming the gain in fiber to optrode coupling efficiency offered by the smaller diameter fibers. A maximum system efficiency of only about 10% is obtained with the 400-μm fiber. Greater system efficiencies can be obtained using light sources with effective emission apertures smaller than 400 μm.

Improvements such as AR coating, focusing/collimating the input beams and removing the taper will increase the efficiency of the optrode array to a maximum of 64%. Taking into account the actual (i.e., higher) reflectance loss inside the tips and redesigning the tip shape will yield even higher efficiency values.

Acknowledgements

This work was funded by the University of Utah Research Foundation. We also acknowledge support by Lockheed Martin Aculight.

#168581 - $15.00 USD Received 15 May 2012; revised 8 Aug 2012; accepted 10 Aug 2012; published 24 Aug 2012